

# Strong parity-violation effects induced by large-amplitude motions: A quantum-dynamics study of substituted chiral methanols

Ayaki Sunaga<sup>1</sup>

<sup>1</sup>*ELTE, Eötvös Loránd University, Institute of Chemistry,  
Pázmány Péter sétány 1/A 1117 Budapest, Hungary \**

An enhanced mechanism is proposed for the large-amplitude-motion-induced parity-violating frequency by integrating the exact quantum dynamics method with the relativistic electronic structure theory. The torsional wavefunctions and PV frequency shifts are obtained by the exact quantum dynamics method. The potential energy curve and PV energy along the torsional coordinates are calculated using the extended atomic mean-field two-component Hamiltonian. The predicted PV frequency shift for the torsional transition of CFCIBrOH is approximately 100 times larger than that of the conventional C-F stretching mode of CHFClBr. The maximum PV frequency shift (3.2 Hz) is obtained in the CHBrIOH molecule.

## I. INTRODUCTION

What will humans discover after improving the precision of molecular spectra? The advancement of cooling techniques for polyatomic molecules [1–4] can transcend the precision of traditional spectroscopies. Although the rotation-vibrational spectra are mainly generated by electromagnetic interactions, the parity-violating (PV) interaction may split them. The PV interaction was first observed in nuclear beta decay [5], using the optical-rotation technique [6, 7] as well as in atomic forbidden transition due to a nuclear anapole moment [8]. Various molecules have been investigated as will be discussed. However, only the upper limit of the PV frequency shift  $\Delta\nu_{\text{PV}}$  has been reported using a methane-like chiral molecule, CHFClBr [9, 10]. Although the PV energy difference between the enantiomer ( $\Delta E_{\text{PV}}$ ) can appear in the framework of the standard model [11–13], the molecular PV shift may be a probe of cold dark matter [14, 15].

As  $E_{\text{PV}}$  increases rapidly with an increase in the nuclear charge ( $Z$ ) becomes large [16–20] (initially estimated for an atomic case [21]), a naive strategy for enhancing  $\Delta E_{\text{PV}}$  involves incorporating the heaviest possible element into the molecule (e.g., tungsten [22], rhenium [23–25], osmium [26], iridium and bismuth [23], astatine [27], uranium [28]). In practice, however, there is a limit to how heavy an element can be as long as  $Z \leq 118$ ; moreover, some heavy elements are radioactive. Another strategy, such as finding a PV-effect-sensitive molecular species, is significantly important. The enhancement of PV shifts in the vibrational shifts in methane-like chiral cations (e.g.,  $\Delta\nu_{\text{PV}} = 1.8$  Hz in  $\text{CHDBrI}^+$ ) has been recently reported [29].

Large  $E_{\text{PV}}$  variations in large-amplitude motion (LAM) are well-known phenomena, although they are rarely applied to PV shift enhancement. For example, in  $\text{H}_2\text{X}_2$  (where  $\text{X} = \text{O}, \text{S}, \text{Se}, \text{Te}, \text{Po}$ ) molecules,  $E_{\text{PV}}$  as

a function of the dihedral angle ( $\theta$ ) behaves as a sinusoidal curve ( $\sim \sin(2\theta)$ ) [19, 20, 30–33], indicating that  $E_{\text{PV}}$  exhibits maximum and minimum values with different signs in  $0^\circ \leq \theta \leq 180^\circ$ . Therefore, is it possible to design molecules whose initial and final transition states take the minima and maxima ranges of  $E_{\text{PV}}$ ?

To exploit this fascinating property of the  $E_{\text{PV}}$  curve, the torsional vibrational motion, which cannot be described by the conventional harmonic approximation, must be explored. An ideal scenario is that two torsional wavefunctions of the target transition are located over a torsional-angle region with different  $E_{\text{PV}}$  values. However, the  $E_{\text{PV}}$  values are relatively similar for a torsional transition in the case of tetratomic molecules, such as ClSSCl (Figure 2 of Ref. 34) and HOSH (Fig. 2 of Ref. 35). Another example of torsional motion is the internal rotation of the methyl unit. Notably, Berger *et al.* reported the one-dimensional (1D) calculation of a methanol isotopomer (HDTCOH), although the maximum PV shift was approximately  $6 \times 10^{-5}$  Hz [36]. A heavier molecule, including a torsional motion (GeClBrI-CF<sub>3</sub>), was calculated [23], although it is fixed at the optimized structure, and its torsional motion was not investigated.

Here, the PV shift in the torsional motions of the CXYZ unit in CXYZOH ( $\text{X}, \text{Y}, \text{Z} = \text{H}, \text{F}, \text{Cl}, \text{Br}, \text{I}$ ) molecules was investigated. Strong PV enhancements are observed due to the localization of the torsional wavefunction to the geometries exhibiting opposite  $\Delta E_{\text{PV}}$  signs. The results obtained for CHBrIOH, CFBrIOH, CFCIBrOH, and CClBrIOH molecules are reported as examples, and those for the other molecular species are reported in the Supplementary Material (SM).

## II. THEORY

Figure 1 shows the flow diagram for obtaining the PV frequency of the torsional states.

1. Geometry optimization was performed at each X-C-O-H dihedral angle ( $\tau_1$  in Figure 2). The calculations were performed over an equidistant grid of

\* ayaki.sunaga@ttk.elte.hu,sunagaayaki@gmail.com

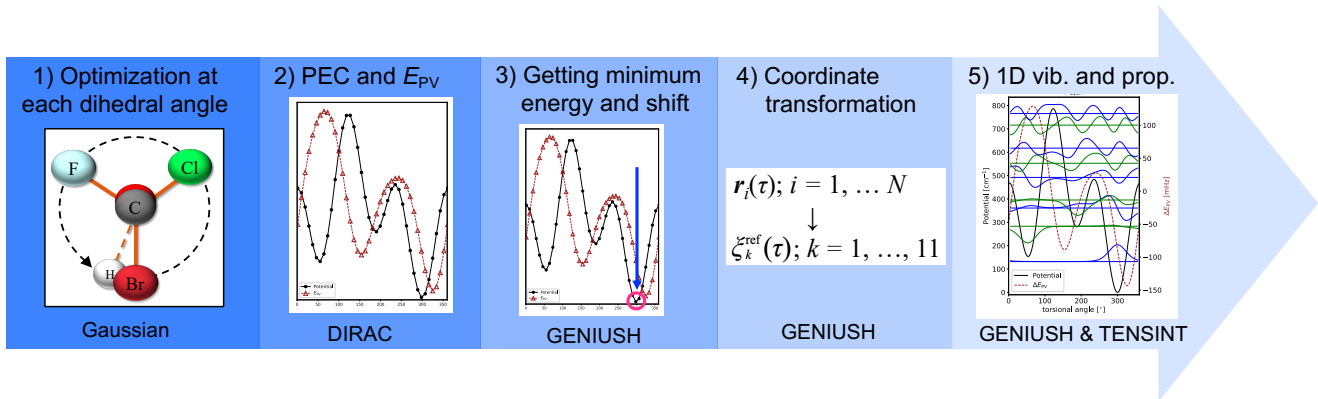


FIG. 1. Overview of the steps for obtaining  $\Delta\nu_{PV}$  for the torsional states of CXYZOH molecules and utilized programs. From the left, 1-2) the electronic structure calculations, 3) energy shift, 4) coordinate transformations, and 5) quantum dynamics calculations are performed. The figure for step 1) shows the direction of the internal rotation of the CXYZ unit and the geometry with  $\tau_1 \approx 10$ .

$\tau$  points,  $\tau_{1,n} = (n - 1)9^\circ$  ( $n = 1, \dots, 41$ ). Figure 3 shows the direction of the internal rotation; CFCIBrOH was used as an example.

- The total energies (the potential energy curve, PEC) and  $\Delta E_{PV}$  were calculated using optimized geometries at  $\tau_{1,n}$  ( $n = 1, \dots, 41$ ; solid black line in Figure 3).
- The minimum energy on the PEC was obtained using the simplex code [37], and the PEC was shifted so that its bottom could become zero  $\text{cm}^{-1}$ .
- The Cartesian coordinates optimized in Step 1 with respect to  $\tau_1$  were transformed into the relaxed reference internal coordinates. First, we extracted  $\tau_1, \tau_2$ , and  $\tau_3$  from the Cartesian coordinate defined in Eq. 1 and obtain the torsional angle ( $\tau$ ; Eq. 2). Further,  $\xi_k^{\text{ref}}(\tau_n)$  ( $n = 1, 2, \dots, 37$ , which covers  $0^\circ \leq \tau \leq 360^\circ$ ) is obtained from  $\mathbf{r}_i^{\text{ref}}(\tau_n)$ , and these discrete coordinates  $\xi_k^{\text{ref}}(\tau_n)$  are interpolated to obtain  $\xi_k^{\text{ref}}(\tau)$ . Additionally, the horizontal axis of the potential energy is also transformed ( $V(\tau_{1,n}) \rightarrow V(\tau_n)$ ), while  $V(\tau_n)$  is interpolated.
- A 1D vibration calculations (considering only the torsional motion) was performed, and  $\Delta\nu_{PV}$  at each torsional state was obtained using the expectation value with respect to the vibrational wavefunction (Figure 4 and Table I)

The following definition was used to obtain the body-fixed Cartesian coordinate (Figure 2), following Ref. 37

$$\mathbf{r}_C = \mathbf{0}, \quad \mathbf{r}_O = \begin{pmatrix} 0 \\ 0 \\ r_1 \end{pmatrix}, \quad (1)$$

$$\mathbf{r}_H = \mathbf{r}_O + \begin{pmatrix} 0 \\ r_2 \cos(\theta_1 - \pi/2) \\ r_2 \sin(\theta_1 - \pi/2) \end{pmatrix},$$

$$\mathbf{r}_Z = \begin{pmatrix} -r_3 \sin \theta_2 \sin \tau_1 \\ r_3 \sin \theta_2 \cos \tau_1 \\ r_3 \cos \theta_2 \end{pmatrix}, \quad \mathbf{r}_Y = \begin{pmatrix} -r_4 \sin \theta_3 \sin \tau_2 \\ r_4 \sin \theta_3 \cos \tau_2 \\ r_4 \cos \theta_3 \end{pmatrix},$$

$$\mathbf{r}_X = \begin{pmatrix} -r_5 \sin \theta_4 \sin \tau_3 \\ r_5 \sin \theta_4 \cos \tau_3 \\ r_5 \cos \theta_4 \end{pmatrix},$$

where the atomic number increases from atoms X-Z. The frame for the internal rotation of the CXYZ unit was also defined based on the body-fixed Cartesian coordinate definition (Eq. 1). Furthermore, the center of mass was fixed at the origin of the body-fixed coordinate system, which offers an additional constant shift vector to each vector in Eq. 1. These coordinate definitions were used in the vibrational calculations to prevent the rotation of the frame.

The electronic structure calculations, including geometry optimization, PEC, and  $\Delta E_{PV}$  calculations, were performed on structures parametrized by H-C-O-Z dihedral angle,  $\tau_1$ , whereas the torsional motion in the quantum dynamics calculation was described by  $\tau$ , defined as a linear combination of  $\tau_1, \tau_2$ , and  $\tau_3$

$$\tau = \frac{1}{3} (\tau_1 + \tau_2 + \tau_3), \quad (2)$$

$$\varphi_1 = \frac{1}{\sqrt{2}} (\tau_2 - \tau_3), \quad \varphi_2 = \frac{1}{\sqrt{6}} (2\tau_1 - \tau_2 - \tau_3).$$

This definition facilitated the identification of  $\tau$  as the single LAM in the system, with the  $\varphi_1, \varphi_2$  small-amplitude motions (SAMs). This extraction technique

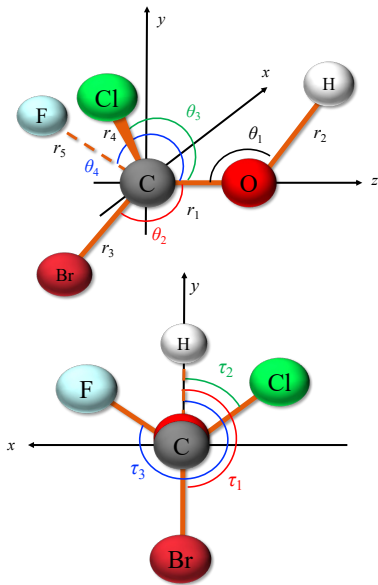


FIG. 2. Visualization of a CXYZOH molecule (*S*-CFCIBrOH as an example) and the primitive internal coordinates in the right-handed body-fixed Cartesian frame. In the configuration of this figure,  $\tau_1 = 180^\circ$ .

for  $\tau$  was initially proposed in Refs. [38, 39]. For subsequent convenience, we define the following compact notation for the internal coordinates,

$$\boldsymbol{\rho} = (\boldsymbol{\xi}; \tau) = (r_1, r_2, r_3, r_4, r_5, \theta_1, \theta_2, \theta_3, \theta_4, \varphi_1, \varphi_2; \tau), \quad (3)$$

where  $\boldsymbol{\xi}$  collects the SAMs. The mathematically allowed coordinate ranges are defined as  $\tau \in [0, 2\pi)$ , and the other coordinates are inactive in this study.

### A. Vibrational Hamiltonian

The Hamiltonian used to describe the quantum vibrational motion can be expressed in the Podolsky form [40]:

$$\hat{H}^{\text{rv,P}} = \frac{1}{2} \sum_{k=1}^D \sum_{l=1}^D \tilde{g}^{-1/4} \hat{p}_k \tilde{g}^{1/2} G_{kl} \hat{p}_l \tilde{g}^{-1/4} + V, \quad (4)$$

where  $D$  is the number of the vibrational degree of freedom in the molecule,  $\hat{p}_k = -i\partial/\partial\rho_k$  is the momentum operator with respect to the internal coordinates,  $\tilde{g} = \det(\mathbf{g})$ ,  $\mathbf{G} = \mathbf{g}^{-1}$ , and  $V$  is the potential energy depending on the coordinates of the nuclei. In our vibrational calculations, we considered only the torsional motion (i.e.,  $D = 1$ ). In the GENIUSH program [41, 42], the mass-weighted metric tensor,  $\mathbf{g}$ , was calculated from the  $t$ -vectors, as follows:

$$g_{kl} = \sum_{i=1}^N m_i \mathbf{t}_{ik}^T \mathbf{t}_{il}, \quad (5)$$

with the vibrational  $t$ -vector:

$$\mathbf{t}_{ik} = \frac{\partial \mathbf{r}_i}{\partial \rho_k}, \quad k = 1, 2, \dots, D, \quad (6)$$

and the rotational  $t$ -vector:

$$\mathbf{t}_{iD+a} = \mathbf{e}_a \times \mathbf{r}_i, \quad a = 1(x), 2(y), 3(z), \quad (7)$$

where  $\mathbf{e}_a$  is the unit vector in the body-fixed Cartesian coordinates. In the actual calculations, the  $t$ -vectors are obtained at the discrete-variable representation (DVR) grid points ( $\tau_\alpha = 1, \dots, 37$ ), i.e., the matrix elements are constructed based on  $\mathbf{r}_{i\alpha}$  rather than  $\mathbf{r}_i$  in eqs 6 and 7. The reference internal coordinates for obtaining  $\mathbf{r}_{i\alpha}$  are relaxed at each  $\tau_\alpha$  [ $\boldsymbol{\xi}^{\text{ref}}(\tau_\alpha)$ ], where  $\boldsymbol{\xi}^{\text{ref}}(\tau_\alpha)$  is the geometry that minimizes  $V$  at a given  $\tau$ ,  $\tau_\alpha$ . Employing the relaxed coordinates indicates that the moment of inertia in this study depends on  $\tau$ . The wavefunctions and energies associated with Eq. 4 are obtained in a variational manner.

### B. Parity-violating Hamiltonian

The PV effective Hamiltonians arise from the coupling between the vector [ $V; \psi^\dagger(\boldsymbol{\alpha}, \mathbf{i})\psi$ ] and axial-vector [ $A; \psi^\dagger(\boldsymbol{\Sigma}, \boldsymbol{\gamma})\psi$ ] terms of the Fermion currents [11, 20, 43, 44]. Employing indices of an electron (e) and a nucleon [proton (p) and nucleon (n)],  $V_e - A_{p,n}$  and  $A_e - V_{p,n}$  contribute to the nuclear spin-dependent term and independent term, respectively. The former could appear in nuclear magnetic resonance (NMR) [45–48] owing to the contribution from the nuclear spin ( $\psi_{p,n}^\dagger \boldsymbol{\Sigma} \psi_{p,n}$ ). The latter is our target, where the effective Hamiltonian in the four-component framework is shown as [11, 20, 43, 44]

$$\hat{H}_{\text{PV}} = \frac{G_{\text{F}}}{2\sqrt{2}} \sum_A Q_{W,A} \sum_i \gamma_i^5 \rho_A (\mathbf{r}_i - \mathbf{r}_A). \quad (8)$$

Here,  $G_{\text{F}} = 2.22255 \times 10^{-14} E_h a_0^3$  is the Fermi coupling constant,  $Q_{W,A} = -N_A + Z_A(1 - 4 \sin^2 \theta_W)$  is the weak charge of the nucleus  $A$ , with its neutron number  $N_A$  and nuclear charge  $Z_A$ . The Weinberg mixing angle  $\theta_W = 0.2319$  [49, 50] was also employed.  $\gamma^5 = -i\gamma^0\gamma^1\gamma^2\gamma^3$  is the Dirac matrix that results in the coupling between the large and small components of the wavefunction. Additionally,  $\rho_A$  is the charge density of nucleus  $A$  for which the Gaussian-type model [51] is employed in this study. As the PV interaction is mediated by the heavy  $Z_0$  boson, the contact interaction between  $\rho_A$  and an electron offers a good approximation. Although Eq. 8 is a four-component expression, it is numerically transformed into a two-component framework (picture-change [52]) in this study. As the sign of the  $\hat{H}_{\text{PV}}$  becomes opposite after parity inversion, the energy difference due to the PV interaction between the *R*- and *S*-configuration can be expressed by

$$\Delta E_{\text{PV}} = 2E_{\text{PV}}^Z; \quad E_{\text{PV}} = \langle \Psi_e^Z | \hat{H}_{\text{PV}} | \Psi_e^Z \rangle. \quad (9)$$

where  $Z$  is the target configuration of the molecule ( $R$  or  $S$ ).  $E_{\text{PV}}$  is the PV energy obtained from the expectation value with respect to the electronic wavefunction,  $\Psi_e$ . The PV shift at the vibrational state,  $|\Psi_\nu\rangle$ , is given, as follows:

$$\Delta\nu_{\text{PV},\nu} = \langle \Psi_\nu | \Delta E_{\text{PV}}(\boldsymbol{\rho}) | \Psi_\nu \rangle, \quad (10)$$

where  $\Delta E_{\text{PV}}(\boldsymbol{\rho})$  expresses the value of  $E_{\text{PV}}$  at the nuclear configuration,  $\boldsymbol{\rho}$ . We obtained the expected value with respect to the DVR vibrational wavefunction. This indicates that the error due to the truncation of the potential (e.g., the harmonic oscillator and anharmonic correction), which is traditionally employed in this field, is not observed in this manner.

### III. COMPUTATIONAL DETAILS

The vibrational Schrödinger equation in a reduced-dimension form was solved using the GENIUSH program [41, 42], which was recently reviewed in Ref. 53. The derivative in Eq. 6 was obtained numerically (two-point central derivative) using the step size  $1.0 \times 10^{-5}$  bohr. Furthermore, 37 Fourier-DVR grid points, which is a sufficient number of grid points as presented in Table S1 of the SM, were used to solve the vibrational Schrödinger equation. The TENSINT program [54, 55] was used to obtain  $\Delta\nu_{\text{PV}}$  at each torsional energy level.

Geometry optimization was carried out using the Gaussian16 software package [56]. For the Br and I atoms, we employed the pseudopotentials ECP10MDF and ECP28MDF, respectively, and the cc-pVTZ-PP basis sets [57, 58]. For the H, C, O, F, and Cl atoms, we employed the Def2TZVPP basis sets [59]. The PBE1PBE functional [60, 61] was used for the density functional theory (DFT) functional. Dispersion effects were considered within the semi-empirical D3 van der Waals corrections [62].

To calculate the total electronic energy and  $\Delta E_{\text{PV}}$ , we employed a development version (git hash: 3970bcf) of the DIRAC program package [63, 64]. We constructed a two-component relativistic Hamiltonian using the exact two-component (X2C) Hamiltonian [65] for the one-electron operators and the extended atomic mean-field (eAMF-X2C) approach [66] to consider the picture-change effect of the two-electron Coulomb and Gaunt terms. The PBE0 functionals [60, 61] were employed for the electronic structure calculations, and the dyall.3zp basis sets [67–69] were employed for all the elements in the molecules in the uncontracted form. Several tight exponents, which were optimized using the simplex method [70], were also added (Table S2 of the SM). The Gaussian-type finite nuclear-charge model [51] was employed for the relativistic calculations.

### IV. RESULTS AND DISCUSSION

Figure 3 shows the criticality of the geometry-relaxation effect in the generation of the 1D PEC and  $\Delta E_{\text{PV}}$  curve. The fixed-geometry model cannot reproduce the results of the relaxed structure, as some wells in the PEC do not appear in the fixed-geometry model. Although the situation is better in  $\Delta E_{\text{PV}}$ , the fixed-geometry model overestimates the PV sensitivities in many regions. From a different perspective, geometries deviating from the optimized torsional path can display larger PV sensitivities, and it encourages full-dimensional quantum dynamics calculations in future studies. The relaxed structure model was used for the following discussion. Although the shape of the  $\Delta E_{\text{PV}}$  curve appeared complicated, two sinusoidal curves (a local minimum and a local maximum at  $0^\circ$ - $180^\circ$  and  $180^\circ$ - $360^\circ$ , respectively) can be found for some target molecules (see Figures 4 and S1-S6 in the SM).

The enhancement of the PV frequency shift induced by the torsional motion can be visually demonstrated. Figure 4 shows the PEC,  $\Delta E_{\text{PV}}$  curve, and torsional wavefunctions of some CXYZOH molecules. The  $\Delta E_{\text{PV}}$  curves take various values along  $\tau$ , and the torsional wavefunctions located in different wells can exhibit different  $\Delta E_{\text{PV}}$  values. This yields large  $\Delta\nu_{\text{PV}}$  values in the transition across the two wells. This is in contrast to SAMs, where the small displacement from the equilibrium structure contributes to the vibrational wavefunction, and the two states exhibit a similar  $\Delta\nu_{\text{PV}}$  magnitude. Following Ref. 29, the contribution from the  $\partial^2 E_{\text{PV}}(q)/\partial q^2|_{q=0} \approx 0$  term is small, yielding a linear-like  $\Delta E_{\text{PV}}$  curve with respect to the vibrational coordinate ( $q$ ). The  $\Delta\nu_{\text{PV}}$  value and vibrational band origin for each torsional state are presented in Table I. Assuming the state control was possible, the maximum sensitivity of 3.2 Hz would be achieved in CHBrIOH. The PV frequencies from the ground state exceeded more than 1.0 Hz in the transitions of the CHBrIOH and CFBrIOH molecules. Compared with the CHFClBr molecule with  $\Delta\nu_{\text{PV}} = 1.867$  (-3.781) mHz for the C-F stretching (FCCl bending) fundamental modes [71], approximately 100- (50-)fold enhancement was observed in CFClBrOH (186.4 mHz) without including a heavy element. The necessary precisions (the ratio between the PV shift and torsional frequency) for detecting the PV shift are  $\sim 4 \times 10^{-12}$  and  $\sim 1 \times 10^{-14}$  for CHBrIOH and CFClBrOH, respectively.

These PV enhancements would not be due to the approximation employed in this study. The qualitative accuracy of the reduced dimensional models that consider only large-amplitude motion(s) has been confirmed in previous studies [41, 72–75]. The PBE0 functional offers an acceptable quality (maximum absolute error of 0.5 kcal/mol from the CCSD(T) level) for the torsional potential energy including halogens (Figure 5 of ref [76]). The torsional coordinates that offer the maximum, zero, and minimum  $E_{\text{PV}}$  values do not significantly depend

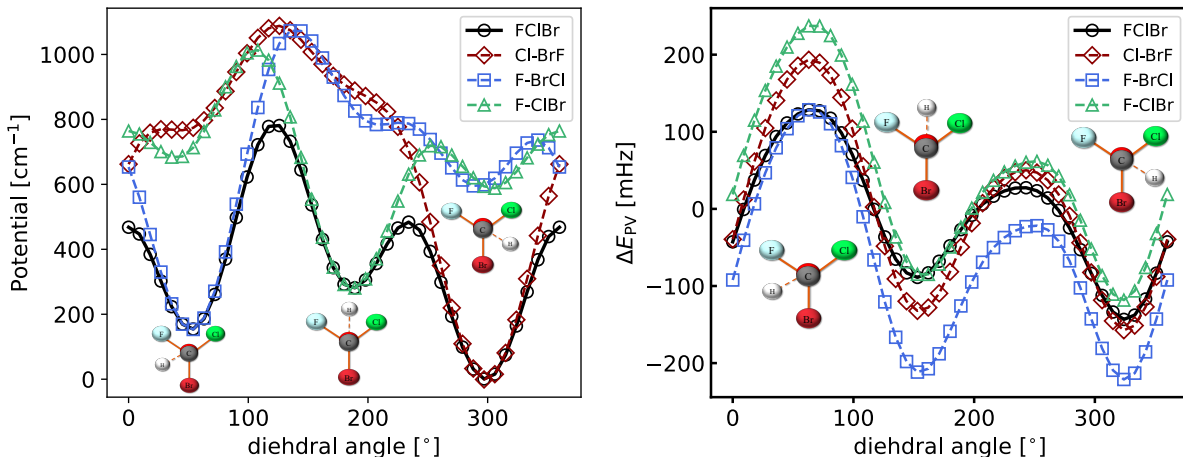


FIG. 3. PECs (left) and  $\Delta E_{PV}$  curves (right) of *S*-CFCIBrOH obtained under various geometry-optimization conditions. The solid black line (FCIBr) indicates that the geometry optimization was performed at all the grid points (dihedral angle,  $\tau_{1,n}$  ( $n = 1, \dots, 41$ )). The dotted line (legend A-BC) indicates that the geometries were optimized using an initial structure in which the hydrogen of the OH group is positioned between atoms A and B at the PBE1PBE-D3/cc-pVTZ level. The internal coordinates were fixed to generate the PECs. The molecular figures show the schematic configurations around  $\tau_1 = 60^\circ, 180^\circ, 300^\circ$ . The PBE0 functional based on the eAMF-X2C Hamiltonian and dyall.3zp basis sets with tight exponents were employed to calculate the PECs and  $\Delta E_{PV}$  curves.

on the methodology choice, e.g., the sinusoidal curves of  $H_2X_2$  (Fig. 1 of Ref. 20), and the torsional curves of dichlorinedioxide and substituted allenes [77]. Although the maximum and minimum  $E_{PV}$  values depend on the methodology, the error due to PBE0 would be much smaller than the enhancement, as the maximum difference between  $E_{PV}$  at the PBE0 and CCSD levels of theory is approximately 11% for the  $H_2X_2$  ( $X = O, S, Se, Te, Po$ ) molecules [70]. The PV enhancement due to the torsional motion was also observed with the CAM-B3LYP\* functional [78], as shown in Sec S6 of the SM.

Another advantage of the transitions across the well is that the extremely long lifetime of the torsional excited states is expected. When the torsional wavefunctions are mainly localized to one of the three wells, they may be recognized as exhibiting different vibrational modes from one that is localized to another well. For example, the localized torsional states of #1, #2, and #3 of CCIBrIOH can be assigned to hypothetical vibrational modes with different quantum numbers,  $\nu_{Cl}$ ,  $\nu_I$  and  $\nu_{Br}$ . These nearly forbidden transitions produce a long lifetime of the vibrational excited states, resulting in a very narrow line width for the transition.

Some torsional transitions appear in the terahertz (THz) range, where lasers are actively developed to achieve stable frequencies [79], as in the case of quantum cascade lasers [80, 81]. However, the transition to the SAM-LAM coupling mode can reach the wavelengths in the infrared range, where  $CO_2$  laser can reach. In the case of the H-containing species, PV-sensitive transitions are observed in the infrared range, such as the transition between #1 and #5 of CHBrIOH presented in Table I. To the best of our knowledge, these substituted methanol

TABLE I. Vibrational energies ( $\tilde{\nu}$  in  $cm^{-1}$ ) referenced to the zero-point vibrational energy (#1) and PV frequency shift ( $\Delta\nu_{PV}$  in mHz) of the *R*-CHBrIOH, *S*-CFBrIOH, *S*-CFCIBrOH, and *S*-CCIBrIOH Molecules.  $\nu_A$  ( $A = X, Y, Z$ ) is the quantum number for the well in which the dihedral angle X-C-O-H is close to  $180^\circ$  at the approximately corresponding  $\tau$  values (in degree). The  $\nu_A$  represents the torsional quantum number, which is detailed in Sec. S5 of the SM. “-” refers to the mixed states that are delocalized to the three wells. The recommended transition is highlighted in bold.

$\tau$	60	180	300	CHBrIOH	$\tau$	60	180	300	CFBrIOH		
#	$\nu_{Br}$	$\nu_I$	$\nu_H$	$\tilde{\nu}$	$\Delta\nu_{PV}$	#	$\nu_{Br}$	$\nu_I$	$\nu_F$	$\tilde{\nu}$	$\Delta\nu_{PV}$
1	0	0	1	191	-259.7	1	0	0	1	144	<b>-674.1</b>
2	0	0	2	376	-402.7	2	0	1	0	224	-682.2
3	0	0	3	710	-547.3	3	0	1	2	260	-638.1
4	0	0	4	990	-746.6	4	1	0	0	317	<b>672.7</b>
5	0	1	4	1115	<b>1556.9</b>	5	0	2	2	417	-483.5
6	1	1	5	1190	-1277.0	6	0	2	3	484	-725.5
7	1	1	5	1218	<b>-1629.4</b>	7	-	-	-	529	204.8
8	1	2	5	1320	474.2	8	-	-	-	629	-404.7
9	-	-	-	1358	-578.0	9	-	-	-	665	-172.5

$\tau$	60	180	300	CFCIBrOH	$\tau$	60	180	300	CCIBrIOH		
#	$\nu_{Cl}$	$\nu_{Br}$	$\nu_F$	$\tilde{\nu}$	$\Delta\nu_{PV}$	#	$\nu_{Br}$	$\nu_I$	$\nu_{Cl}$	$\tilde{\nu}$	$\Delta\nu_{PV}$
1	0	0	1	132	<b>-82.2</b>	1	0	0	1	155	<b>-479.5</b>
2	1	0	0	151	<b>104.2</b>	2	0	1	0	37	-168.0
3	0	0	2	229	-54.4	3	1	0	0	133	<b>367.0</b>
4	0	1	2	264	-33.4	4	0	2	2	267	-364.4
5	2	0	3	360	22.4	5	0	2	2	284	-319.1
6	-	-	-	421	5.2	6	2	2	0	364	332.7
7	-	-	-	486	-21.1	7	-	-	-	442	-301.3
8	-	-	-	584	-0.8	8	-	-	-	524	-234.6
9	-	-	-	634	-9.0	9	-	-	-	559	-58.1

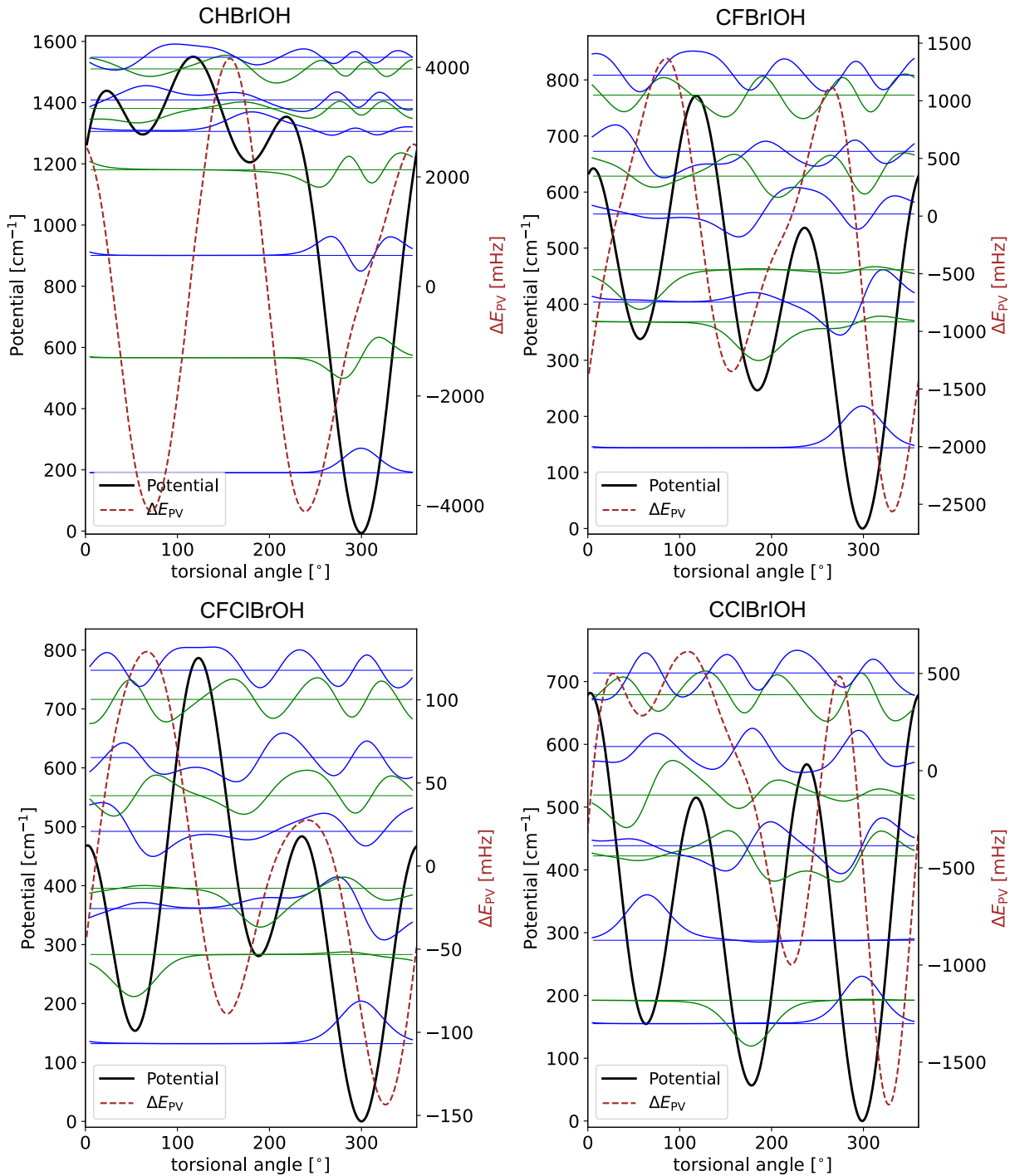


FIG. 4. Visualization of the PECs (black solid line; left axis), 1D torsional wavefunctions (left axis), and  $\Delta E_{PV}$  curves (brown dotted line; right axis) of the *R*-CHBrIOH, *S*-CFBrIOH, *S*-CFCIBrOH, and *S*-CCIBrIOH molecules. The blue and green solid lines indicate the odd (ground, 3rd, ...) and even-numbered (2nd, 4th, ...) levels of the torsional states. The horizontal axis is  $\tau$  defined in Eq. 2.  $\Delta \nu_{PV}$  at each torsional level is presented in Table I.

molecules have not been synthesized; however, they may be formulated in the gas phase via laser ablation, which is widely employed (e.g., Refs. 82–86).

## V. CONCLUSIONS

In conclusion, an enhancement mechanism for the PV frequency originating in the torsional motions of substi-

tuted chiral methanol molecules was demonstrated. The torsional transition of the CFCIBrOH molecule exhibits approximately 100 times more sensitivity to the PV measurement compared with the conventional C-F stretching motion of the CHFCIBr molecule. The calculated PV shift of CHBrIOH reached 3.2 Hz. The torsional energy levels were calculated using the exact quantum dynamics method. The PECs and  $\Delta E_{PV}$  curves of the torsional motion were calculated using a DFT method based on the two-component relativistic eAMF-X2C Hamiltonian. The key idea of the enhancement mechanism is that the torsional states located in different wells can have  $\Delta\nu_{PV}$  with the opposite sign.

The insights from this study are general and could be combined with other existing ideas, e.g., including heavier elements in the molecule and cationic systems [29]. A similar enhancement is expected in the PV NMR shielding constant as this property in  $\text{H}_2\text{O}_2$  yields shows a sinusoidal curve [46, 47]. This study aims to demonstrate the enhancement mechanism of the PV effect. These molecules should be pursued with more accurate calculations, e.g., quantum dynamics calculations taking the full dimension into account, which were demonstrated in methanol [37], as well as electron-correlated calculations

for the PEC and PV curve. Our enhancement mechanism also encourages the development of lasers in the THz range.

## ACKNOWLEDGMENTS

The author wishes to acknowledge a financial support from the European Union's Horizon 2022 research and innovation programme under the Marie Skłodowska-Curie Grant Agreement No. 101105452 (QDMAP) and the JSPS KAKENHI (grant no 21K14643). The author used the computer resource offered under the category of General Projects by the Research Institute for Information Technology, Kyushu University, and the FUJITSU Supercomputer PRIMEHPC FX1000 and FUJITSU Server PRIMERGY GX2570 (Wisteria/BDEC-01) at the Information Technology Center, The University of Tokyo. The author thanks Edit Mátyus (Budapest) for valuable discussions and Alberto Martín Santa Daría (Salamanca) for the support in adding the PV module to the TENSINT code. The author thanks Editage ([www.editage.com](http://www.editage.com)) for English language editing.

- 
- [1] Y. Miyamoto, R. Tobaru, Y. Takahashi, A. Hiramoto, K. Iwakuni, S. Kuma, K. Enomoto, and M. Baba, High-resolution spectroscopy of buffer-gas-cooled phthalocyanine, *Commun Chem* **5**, 161 (2022).
- [2] R. Aiello, V. Di Sarno, M. G. Delli Santi, M. De Rosa, I. Ricciardi, P. De Natale, L. Santamaria, G. Giusfredi, and P. Maddaloni, Absolute frequency metrology of buffer-gas-cooled molecular spectra at 1 kHz accuracy level, *Nat. Commun.* **13**, 7016 (2022).
- [3] L. Anderegg, N. B. Vilas, C. Hallas, P. Robichaud, A. Jadbabaie, J. M. Doyle, and N. R. Hutzler, Quantum control of trapped polyatomic molecules for eEDM searches, *Science* **382**, 665 (2023).
- [4] N. B. Vilas, P. Robichaud, C. Hallas, G. K. Li, L. Anderegg, and J. M. Doyle, An optical tweezer array of ultracold polyatomic molecules, *Nature* **628**, 282 (2024).
- [5] C. S. Wu, E. Ambler, R. W. Hayward, D. D. Hoppes, and R. P. Hudson, Experimental test of parity conservation in beta decay, *Physical Review* **105**, 1413 (1957).
- [6] L. M. Barkov and M. Zolotarev, Observation of parity nonconservation in atomic transitions, *JETP Lett.* **27**, 357 (1978).
- [7] L. M. Barkov and M. S. Zolotarev, Parity violation in atomic bismuth, *Phys. Lett. B* **85**, 308 (1979).
- [8] C. S. Wood, S. C. Bennett, D. Cho, B. P. Masterson, J. L. Roberts, C. E. Tanner, and C. E. Wieman, Measurement of parity nonconservation and an anapole moment in cesium, *Science* **275**, 1759 (1997).
- [9] C. Daussy, T. Marrel, A. Amy-Klein, C. T. Nguyen, C. J. Bordé, and C. Chardonnet, Limit on the parity nonconserving energy difference between the enantiomers of a chiral molecule by laser spectroscopy, *Phys. Rev. Lett.* **83**, 1554 (1999).
- [10] M. Ziskind, C. Daussy, T. Marrel, and C. Chardonnet, Improved sensitivity in the search for a parity-violating energy difference in the vibrational spectrum of the enantiomers of CHFCIBr, *Eur. Phys. J. D* **20**, 219 (2002).
- [11] R. Berger, Parity-violation effects in molecules, in *Theoretical and Computational Chemistry*, Vol. 14 (Elsevier, 2004) pp. 188–288.
- [12] M. Quack, J. Stohner, and M. Willeke, High-resolution spectroscopic studies and theory of parity violation in chiral molecules, *Annu. Rev. Phys. Chem.* **59**, 741 (2008).
- [13] R. Berger and J. Stohner, Parity violation, *Wiley Interdiscip. Rev. Comput. Mol. Sci.* **9**, 1 (2019).
- [14] P. Bargeño, A. Dobado, and I. Gonzalo, Could dark matter or neutrinos discriminate between the enantiomers of a chiral molecule?, *EPL* **82**, 13002 (2008).
- [15] K. Gaul, M. G. Kozlov, T. A. Isaev, and R. Berger, Chiral molecules as sensitive probes for direct detection of P-odd cosmic fields, *Phys. Rev. Lett.* **125**, 123004 (2020).
- [16] I. B. Zel'dovich, Energy difference between right-hand and left-hand molecules, due to parity nonconservation in weak interactions of electrons with nuclei, *Pis'ma Zh. Eksp. Toer. Fiz.* **25**, 106 (1977).
- [17] D. W. Rein, R. A. Hegstrom, and P. G. H. Sandars, Parity non-conserving energy difference between mirror image molecules, *Phys. Lett. A* **71**, 499 (1979).
- [18] R. A. Hegstrom, D. W. Rein, and P. G. H. Sandars, Calculation of the parity nonconserving energy difference between mirror-image molecules, *J. Chem. Phys.* **73**, 2329 (1980).
- [19] J. K. Laerdahl and P. Schwerdtfeger, Fully relativistic ab initio calculations of the energies of chiral molecules including parity-violating weak interactions, *Phys. Rev. A* **60**, 4439 (1999).

- [20] R. Bast, A. Koers, A. S. P. Gomes, M. Iliáš, L. Visscher, P. Schwerdtfeger, and T. Saue, Analysis of parity violation in chiral molecules, *Phys. Chem. Chem. Phys.* **13**, 864 (2011).
- [21] Bouchiat and C. Bouchiat, I. parity violation induced by weak neutral currents in atomic physics, *Journal De Physique* **35**, 899 (1974).
- [22] D. Figgen, T. Saue, and P. Schwerdtfeger, Relativistic four- and two-component calculations of parity violation effects in chiral tungsten molecules of the form NWXYZ (X, Y, Z=H, F, Cl, Br, or I), *J. Chem. Phys.* **132**, 10.1063/1.3439692 (2010).
- [23] P. Schwerdtfeger, J. Gierlich, and T. Bollwein, Large parity-violation effects in heavy-metal-containing chiral compounds, *Angew. Chem. Int. Ed Engl.* **42**, 1293 (2003).
- [24] N. Saleh, R. Bast, N. Vanthuyne, C. Roussel, T. Saue, B. Darquié, and J. Crassous, An oxorhenium complex bearing a chiral cyclohexane-1-olato-2-thiolato ligand: Synthesis, stereochemistry, and theoretical study of parity violation vibrational frequency shifts, *Chirality* **30**, 147 (2018).
- [25] N. Sahu, K. Gaul, A. Wilm, M. Schnell, and R. Berger, Towards detection of molecular parity violation by microwave spectroscopy of  $\text{CpRe}(\text{CH}_3)(\text{CO})(\text{NO})$ , arXiv: 2303.08263 [physics.chem-ph] (2023).
- [26] M. R. Fiechter, P. A. B. Haase, N. Saleh, P. Soulard, B. Tremblay, R. W. A. Havenith, R. G. E. Timmermans, P. Schwerdtfeger, J. Crassous, B. Darquié, L. F. Pašteka, and A. Borschevsky, Toward detection of the molecular parity violation in chiral  $\text{ru}(\text{acac})_3$  and  $\text{os}(\text{acac})_3$ , *J. Phys. Chem. Lett.* **13**, 10011 (2022).
- [27] R. Berger and J. L. Stuber, Electroweak interactions in chiral molecules: two-component density functional theory study of vibrational frequency shifts in polyhalomethanes, *Mol. Phys.* **105**, 41 (2007).
- [28] M. Wormit, M. Olejniczak, A.-L. Deppenmeier, A. Borschevsky, T. Saue, and P. Schwerdtfeger, Strong enhancement of parity violation effects in chiral uranium compounds, *Phys. Chem. Chem. Phys.* **16**, 17043 (2014).
- [29] Eduardus, Y. Shagam, A. Landau, S. Faraji, P. Schwerdtfeger, A. Borschevsky, and L. F. Pašteka, Large vibrationally induced parity violation effects in  $\text{CHDBrI}^+$ , *Chem. Commun.* **59**, 14579 (2023).
- [30] P. Lazzeretti and R. Zanasi, On the calculation of parity-violating energies in hydrogen peroxide and hydrogen disulphide molecules within the random-phase approximation, *Chem. Phys. Lett.* **279**, 349 (1997).
- [31] A. Bakasov, T. Ha, and M. Quack, Ab initio calculation of molecular energies including parity violating interactions, *J. Chem. Phys.* **109**, 7263 (1998).
- [32] J. Thyssen, J. K. Laerdahl, and P. Schwerdtfeger, Fully relativistic coupled cluster treatment for parity-violating energy differences in molecules, *Phys. Rev. Lett.* **85**, 3105 (2000).
- [33] R. Berger and C. Van Willen, Density functional calculations of molecular parity-violating effects within the zeroth-order regular approximation, *J. Chem. Phys.* **122**, 10.1063/1.1869467 (2005).
- [34] R. Berger, M. Gottselig, M. Quack, and M. Willeke, Parity violation dominates the dynamics of chirality in dichlorodisulfane, *Angew. Chem. Int. Ed.* **40**, 4195 (2001).
- [35] M. Quack and M. Willeke, Theory of stereomutation dynamics and parity violation in hydrogen thioperoxide isotopomers  $^{1,2,3}\text{HSO}^{1,2,3}\text{H}$ , *Helv. Chim. Acta* **86**, 1641 (2003).
- [36] R. Berger, M. Quack, A. Sieben, and M. Willeke, Parity-Violating potentials for the torsional motion of methanol ( $\text{CH}_3\text{OH}$ ) and its isotopomers ( $\text{CD}_3\text{OH}$ ,  $^{13}\text{CH}_3\text{OH}$ ,  $\text{CH}_3\text{OD}$ ,  $\text{CH}_3\text{OT}$ ,  $\text{CHD}_2\text{OH}$ , and  $\text{CHD}(\text{TOH})$ ), *Helv. Chim. Acta* **86**, 4048 (2003).
- [37] A. Sunaga, G. Avila, and E. Mátyus, Variational vibrational states of methanol (12D), *J. Chem. Theory Comput.* **20**, 8100 (2024).
- [38] R. Meyer and H. H. Günthard, Internal rotation and vibration in  $\text{CH}_2=\text{CCl}-\text{CH}_2\text{D}$ , *J. Chem. Phys.* **50**, 353 (1969).
- [39] S. Bell, Variation of geometry, vibrational frequencies and zero-point energies with internal rotation, *J. Mol. Struct.* **320**, 125 (1994).
- [40] B. Podolsky, Quantum-Mechanically correct form of hamiltonian function for conservative systems, *Phys. Rev.* **32**, 812 (1928).
- [41] E. Mátyus, G. Czakó, and A. G. Császár, Toward black-box-type full- and reduced-dimensional variational (ro)vibrational computations, *J. Chem. Phys.* **130**, 134112 (2009).
- [42] C. Fábri, E. Mátyus, and A. G. Császár, Rotating full- and reduced-dimensional quantum chemical models of molecules, *J. Chem. Phys.* **134**, 074105 (2011).
- [43] A. N. Moskalev, R. M. Ryndin, and I. B. Khriplovich, Possible lines of research into weak-interaction effects in atomic physics, *Sov. Phys. Usp.* **19**, 220 (1976).
- [44] W. Greiner and B. Muller, *Gauge theory of weak interactions*, Vol. 5 (Springer, 1996).
- [45] A. L. Barra, J. B. Robert, and L. Wiesenfeld, Parity non-conservation and NMR observables. calculation of tl resonance frequency differences in enantiomers, *Phys. Lett. A* **115**, 443 (1986).
- [46] G. Laubender and R. Berger, Electroweak quantum chemistry for nuclear-magnetic-resonance-shielding constants: Impact of electron correlation, *PHYSICAL REVIEW A* **74**, 032105 (2006).
- [47] V. Weijo, R. Bast, P. Manninen, T. Saue, and J. Vaara, Methodological aspects in the calculation of parity-violating effects in nuclear magnetic resonance parameters, *J. Chem. Phys.* **126**, 074107 (2007).
- [48] I. A. Aucar, Y. Chamorro, and A. Borschevsky, Parity-violating contributions to nuclear spin-rotation interactions and to NMR shielding constants in tetrahedral molecules, *Phys. Rev. A* **106**, 062802 (2022).
- [49] 0.2319 is the default value of the version of the DIRAC code employed in this study. The value of depends on the renormarization prescription, see Ref. 50.
- [50] P. A. Zyla, R. M. Barnett, J. Beringer, O. Dahl, A. D Dwyer, E. D Groom, C.-J. Lin, K. S Lugoosky, E. Pianori, J. D Robinson, *et al.*, Review of particle physics (rpp 2020), *Progress of Theoretical and Experimental Physics* **2020**, 1 (2020).
- [51] L. Visscher and K. G. Dyall, Dirac-Fock atomic electronic structure calculations using different nuclear charge distributions, *At. Data Nucl. Data Tables* **67**, 207 (1997).
- [52] E. J. Baerends, W. H. E. Schwarz, P. Schwerdtfeger, and J. G. Snijders, Relativistic atomic orbital contractions and expansions: magnitudes and explanations, *J. Phys. B At. Mol. Opt. Phys.* **23**, 3225 (1990).

- [53] E. Mátyus, A. Martín Santa Daría, and G. Avila, Exact quantum dynamics developments for floppy molecular systems and complexes, *Chem. Commun.* **59**, 366 (2023).
- [54] A. Martín Santa Daría, G. Avila, and E. Matyus, Performance of a black-box-type rovibrational method in comparison with a tailor-made approach: Case study for the methane–water dimer, *The Journal of Chemical Physics* **154**, 224302 (2021).
- [55] A. Martín Santa Daría, G. Avila, and E. Mátyus, Methane dimer rovibrational states and raman transition moments, *Phys. Chem. Chem. Phys.* **26**, 10254 (2024).
- [56] M. J. Frisch, G. W. Trucks, H. B. Schlegel, G. E. Scuseria, M. A. Robb, J. R. Cheeseman, G. Scalmani, V. Barone, G. A. Petersson, H. Nakatsuji, X. Li, M. Caricato, A. V. Marenich, J. Bloino, B. G. Janesko, R. Gomperts, B. Mennucci, H. P. Hratchian, J. V. Ortiz, A. F. Izmaylov, J. L. Sonnenberg, D. Williams-Young, F. Ding, F. Lipparini, F. Egidi, J. Goings, B. Peng, A. Petrone, T. Henderson, D. Ranasinghe, V. G. Zakrzewski, J. Gao, N. Rega, G. Zheng, W. Liang, M. Hada, M. Ehara, K. Toyota, R. Fukuda, J. Hasegawa, M. Ishida, T. Nakajima, Y. Honda, O. Kitao, H. Nakai, T. Vreven, K. Throssell, J. A. Montgomery, Jr., J. E. Peralta, F. Ogliaro, M. J. Bearpark, J. J. Heyd, E. N. Brothers, K. N. Kudin, V. N. Staroverov, T. A. Keith, R. Kobayashi, J. Normand, K. Raghavachari, A. P. Rendell, J. C. Burant, S. S. Iyengar, J. Tomasi, M. Cossi, J. M. Millam, M. Klene, C. Adamo, R. Cammi, J. W. Ochterski, R. L. Martin, K. Morokuma, O. Farkas, J. B. Foresman, and D. J. Fox, *Gaussian 16 Revision A.03* (2016), gaussian Inc. Wallingford CT.
- [57] K. A. Peterson, D. Figgen, E. Goll, H. Stoll, and M. Dolg, Systematically convergent basis sets with relativistic pseudopotentials. II. small-core pseudopotentials and correlation consistent basis sets for the post-d group 16–18 elements, *J. Chem. Phys.* **119**, 11113 (2003).
- [58] K. A. Peterson, B. C. Shepler, D. Figgen, and H. Stoll, On the spectroscopic and thermochemical properties of ClO, BrO, IO, and their anions, *J. Phys. Chem. A* **110**, 13877 (2006).
- [59] F. Weigend and R. Ahlrichs, Balanced basis sets of split valence, triple zeta valence and quadruple zeta valence quality for H to rn: Design and assessment of accuracy, *Phys. Chem. Chem. Phys.* **7**, 3297 (2005).
- [60] C. Adamo and V. Barone, Toward reliable density functional methods without adjustable parameters: The PBE0 model, *J. Chem. Phys.* **110**, 6158 (1999).
- [61] M. Ernzerhof and G. E. Scuseria, Assessment of the Perdew–Burke–Ernzerhof exchange–correlation functional, *J. Chem. Phys.* **110**, 5029 (1999).
- [62] S. Grimme, J. Antony, S. Ehrlich, and H. Krieg, A consistent and accurate ab initio parametrization of density functional dispersion correction (DFT-D) for the 94 elements H–pu, *J. Chem. Phys.* **132**, 154104 (2010).
- [63] T. Saue, R. Bast, A. S. P. Gomes, H. J. A. Jensen, L. Visscher, I. A. Aucar, R. Di Remigio, K. G. Dyall, E. Eliav, E. Fasshauer, *et al.*, The DIRAC code for relativistic molecular calculations, *J. Chem. Phys.* **152**, 204104 (2020).
- [64] DIRAC, a relativistic ab initio electronic structure program, Release DIRAC22 (2022), written by H. J. Aa. Jensen, R. Bast, A. S. P. Gomes, T. Saue and L. Visscher *et al.* (available at <http://dx.doi.org/10.5281/zenodo.6010450>, see also <http://www.diracprogram.org>), accessed Nov. 5, 2022.
- [65] M. Iliaš and T. Saue, An infinite-order two-component relativistic hamiltonian by a simple one-step transformation, *J. Chem. Phys.* **126**, 64102 (2007).
- [66] S. Knecht, M. Repisky, H. J. A. Jensen, and T. Saue, Exact two-component hamiltonians for relativistic quantum chemistry: Two-electron picture-change corrections made simple, *J. Chem. Phys.* **157**, 114106 (2022).
- [67] K. G. Dyall, Relativistic double-zeta, triple-zeta, and quadruple-zeta basis sets for the light elements H–Ar, *Theor. Chem. Acc.* **135**, 128 (2016).
- [68] K. G. Dyall, Relativistic and nonrelativistic finite nucleus optimized triple-zeta basis sets for the 4p, 5p and 6p elements, *Theoretical Chemistry Accounts* **108**, 335–340 (2002).
- [69] K. G. Dyall, Relativistic quadruple-zeta and revised triple-zeta and double-zeta basis sets for the 4p, 5p, and 6p elements, *Theoretical Chemistry Accounts* **115**, 441–447 (2006).
- [70] A. Sunaga and T. Saue, Towards highly accurate calculations of parity violation in chiral molecules: relativistic coupled-cluster theory including QED-effects, *Molecular Physics*, e1974592 (2021).
- [71] G. Rauhut and P. Schwerdtfeger, Parity-violation effects in the vibrational spectra of CHFClBr and CDFClBr, *Phys. Rev. A* **103**, 042819 (2021).
- [72] M. L. Senent, Ab initio determination of the torsional spectra of acetic acid, *Mol. Phys.* **99**, 1311 (2001).
- [73] S. Blasco and D. Lauvergnat, Quantum study of the internal rotation of methanol in full dimensionality (1+11d): a harmonic adiabatic approximation, *Chem. Phys. Lett.* **373**, 344 (2003).
- [74] A. G. Csaszar, V. Szalay, and M. L. Senent, Ab initio torsional potential and transition frequencies of acetaldehyde, *J. Chem. Phys.* **120**, 1203 (2004).
- [75] M. Ragni, A. Lombardi, P. R. P. Barreto, and A. C. P. Bitencourt, Orthogonal coordinates and hyperquantization algorithm. the NH<sub>3</sub> and H<sub>3</sub>O<sup>+</sup> umbrella inversion levels, *J. Phys. Chem. A* **113**, 15355 (2009).
- [76] D. N. Tahchieva, D. Bakowies, R. Ramakrishnan, and O. A. von Lilienfeld, Torsional potentials of glyoxal, oxalyl halides, and their thiocarbonyl derivatives: Challenges for popular density functional approximations, *J. Chem. Theory Comput.* **14**, 4806 (2018).
- [77] L. Horný and M. Quack, Computation of molecular parity violation using the coupled-cluster linear response approach, *Mol. Phys.* **113**, 1768 (2015).
- [78] C. Thierfelder, G. Rauhut, and P. Schwerdtfeger, Relativistic coupled-cluster study of the parity-violation energy shift of CHFClBr, *Phys. Rev. A* **81**, 032513 (2010).
- [79] X. Guo, K. Bertling, B. C. Donose, M. Brünig, A. Cernescu, A. A. Govyadinov, and A. D. Rakić, Terahertz nanoscopy: Advances, challenges, and the road ahead, *Appl. Phys. Rev.* **11**, 10.1063/5.0189061 (2024).
- [80] Y. Zeng, B. Qiang, and Q. J. Wang, Photonic engineering technology for the development of terahertz quantum cascade lasers, *Adv. Opt. Mater.* **8**, 1900573 (2020).
- [81] M. S. Vitiello and A. Tredicucci, Physics and technology of terahertz quantum cascade lasers, *Adv. Phys. X* **6**, 1893809 (2021).
- [82] S. K. Tokunaga, R. J. Hendricks, M. R. Tarbutt, and B. Darquié, High-resolution mid-infrared spectroscopy of buffer-gas-cooled methyltrioxorhenium molecules, *New J.*

- Phys. **19**, 053006 (2017).
- [83] P. Asselin, Y. Berger, T. R. Huet, L. Margulès, R. Motiyenko, R. J. Hendricks, M. R. Tarbutt, S. K. Tokunaga, and B. Darquié, Characterising molecules for fundamental physics: an accurate spectroscopic model of methyltrioxorhenium derived from new infrared and millimetre-wave measurements, *Phys. Chem. Chem. Phys.* **19**, 4576 (2017).
- [84] A. Cournol, M. Manceau, M. Pierens, L. Lecordier, D. B. A. Tran, R. Santagata, B. Argence, A. Goncharov, O. Lopez, M. Abgrall, Y. Le Coq, R. Le Targat, H. Alvarez Martinez, W. K. Lee, D. Xu, P. E. Pottie, R. J. Hendricks, T. E. Wall, J. M. Bieniewska, B. E. Sauer, M. R. Tarbutt, A. Amy-Klein, S. K. Tokunaga, and B. Darquié, A new experiment to test parity symmetry in cold chiral molecules using vibrational spectroscopy, *Quantum Electron.* **49**, 288 (2019).
- [85] B. L. Augenbraun, J. M. Doyle, T. Zelevinsky, and I. Kozyryev, Molecular asymmetry and optical cycling: Laser cooling asymmetric top molecules, *Phys. Rev. X* **10**, 31022 (2020).
- [86] T. D. Persinger, J. Han, A. T. Le, T. C. Steimle, and M. C. Heaven, Electronic spectroscopy and ionization potentials for YbOH and YbOCH<sub>3</sub>, *Phys. Rev. A* **107** (2023).
- [87] K. Dylla, I. Grant, C. Johnson, F. Parpia, and E. Plummer, GRASP: A general-purpose relativistic atomic structure program, *computer physics communications* **55**, 425 (1989).
- [88] A. D. Becke, A new mixing of Hartree–Fock and local density-functional theories, *The Journal of chemical physics* **98**, 1372 (1993).
- [89] P. J. Stephens, F. J. Devlin, C. F. Chabalowski, and M. J. Frisch, Ab Initio Calculation of Vibrational Absorption and Circular Dichroism Spectra Using Density Functional Force Fields, *J. Phys. Chem.* **98**, 11623 (1994).
- [90] T. Yanai, D. P. Tew, and N. C. Handy, A new hybrid exchange–correlation functional using the coulomb-attenuating method (CAM-B3LYP), *Chem. Phys. Lett.* **393**, 51 (2004).

**Supporting Information:**  
**Strong parity-violation effects induced by large-amplitude motions:**  
**A quantum-dynamics study of substituted chiral methanols**

**VI. EMPLOYED MASSES**

In the variational vibration calculation, the following atomic masses were used for the nuclei;  $m_{\text{H}} = 1.007825$  u,  $m_{\text{C}} = 12$  u,  $m_{\text{O}} = 15.994915$  u,  $m_{\text{F}} = 18.998403$  u,  $m_{\text{Cl}} = 34.968853$  u,  $m_{\text{Br}} = 78.918330$  u, and  $m_{\text{I}} = 126.90447$  u.

**VII. CONVERGENCE WITH RESPECT TO THE DVR GRID POINTS**

The convergence with respect to the discrete variable representation (DVR) grid points and functions was tested using the CHFIOH molecule (Table II). We obtained the convergence  $0.1 \text{ cm}^{-1}$  for vibrational energies and  $0.1 \text{ mHz}$  for  $\Delta\nu_{\text{PV}}$  using 37 DVR grid points up to 20th vibrational states. The 37 DVR grid points and functions are employed for the calculations in the main text.

TABLE II. Torsional vibrational energy levels of CHFIOH ( $\tilde{\nu}$  in  $\text{cm}^{-1}$ ), referenced to the ZPVE (#1), and parity-violating (PV) frequency ( $\Delta\nu^{\text{PV}}$  in mHz) for an increasing number of Fourier DVR points and functions,  $M_{\tau}$ .  $\delta_{M_{\tau}} = \tilde{\nu}_{M_{\tau}+2} - \tilde{\nu}_{M_{\tau}}$  in  $\text{cm}^{-1}$  for vibrational energies, and  $\delta_{M_{\tau}} = \Delta\nu_{M_{\tau}+2}^{\text{PV}} - \Delta\nu_{M_{\tau}}^{\text{PV}}$  in mHz for the PV frequencies are also listed.

#	$\tilde{\nu}$				$\Delta\nu^{\text{PV}}$			
	$\delta_{31}$	$\delta_{33}$	$\delta_{35}$	37	$\delta_{31}$	$\delta_{33}$	$\delta_{35}$	37
1	0.0	0.0	0.0	188.2	0.0	0.0	0.0	-603.6
2	0.0	0.0	0.0	357.6	0.0	0.0	0.0	-522.9
3	0.0	0.0	0.0	671.3	0.0	0.0	0.0	-406.4
4	0.0	0.0	0.0	908.9	0.0	0.0	0.0	-63.1
5	0.0	0.0	0.0	963.0	0.0	-0.1	0.0	-154.4
6	0.0	0.0	0.0	1103.2	0.0	0.0	0.0	-125.7
7	0.0	0.0	0.0	1181.1	0.0	0.0	0.0	-166.4
8	0.0	0.0	0.0	1229.7	0.0	0.0	0.0	-172.8
9	0.0	0.0	0.0	1292.5	0.0	0.0	0.0	-225.9
10	0.0	0.0	0.0	1422.9	0.1	0.0	0.0	-181.4
11	0.0	0.0	0.0	1434.3	-0.1	0.0	0.0	-232.0
12	0.0	0.0	0.0	1645.5	-0.2	0.0	0.0	-202.6
13	0.0	0.0	0.0	1647.1	0.2	0.0	0.0	-208.7
14	0.0	0.0	0.0	1915.2	0.0	0.1	-0.1	-206.8
15	0.0	0.0	0.0	1915.4	0.0	-0.1	0.1	-207.4
16	0.0	0.0	0.0	2231.7	-0.2	0.0	0.0	-209.3
17	0.0	0.0	0.0	2231.8	0.2	0.0	0.0	-209.2
18	-0.2	0.0	0.0	2594.0	0.4	-0.1	0.0	-211.2
19	0.2	0.0	0.0	2594.1	-0.3	0.1	0.0	-211.4
20	-1.1	-0.1	0.0	3001.2	1.9	0.2	0.0	-213.0

**VIII. TIGHT EXPONENTS**

The added exponents to the dyall.3zp basis sets are listed in Table III. These tight exponents are key to the accurate description of the wavefunction in the core region. These exponents were optimized to reproduce the PV matrix elements of the numerical calculation using the GRASP code [87] within the 1% error. A more detailed explanation of the optimization procedure is described in ref [70].

**IX. PECS, WAVEFUNCTIONS, AND PV CURVES**

All the target molecules are summarized in Table IV. The configurations (*R*- or *S*-) were determined so that the deepest PEC well is located around  $\tau = 300^\circ$ .

Figures 5-10 display the potential energy curves (PECs), 1D torsional wavefunctions, and parity-violating energy ( $\Delta E_{\text{PV}}$ ) curves of the molecules that are not shown in the main text. In these figures, the blue and green solid lines indicate the odd (ground, 3rd, ...) and even-numbered (2nd, 4th, ...) torsional state levels. The horizontal axis represents the torsional angle ( $\tau$ ) defined in Eq. 2 of the main text. An example of the direction of the internal rotation of the CXYZ unit is shown in FIG. 3 of the main text. The atomic number increases from atom X to Z, and the wells correspond to  $\tau \sim 60^\circ, 180^\circ, 300^\circ$ , respectively, corresponding to  $\tau_2 \approx 180^\circ$  (H-O-C-Y),  $\tau_1 \approx 180^\circ$  (H-O-C-Z), and  $\tau_3 \approx 180^\circ$  (H-O-C-X), respectively.

Tables V-X present the vibrational energies and PV frequencies of the target molecules. In these tables,  $\nu_A$  ( $A = \text{X, Y, Z} = \text{H, F, Cl, Br, I}$ ) represents the quantum number that corresponds to the well where the dihedral angle  $A\text{-C-O-H}$  is close to  $180^\circ$  at the corresponding (approximate)  $\tau$  values ( $\tau \sim 60^\circ, 180^\circ, 300^\circ$ ). “-” refers to mixed states that are delocalized into the three wells.

The CXYZOH molecules can be broadly categorized into the following two types based on their CXYZ units: those with hydrogen (H-containing) and those without hydrogen (H-non-containing). The H-containing molecules may be preferred from the measurement viewpoint because the deep well associated with the hydrogen vibrational frequency, denoted as  $\nu_{\text{H}}$ , allows for high-energy transitions achievable by a  $\text{CO}_2$  laser (around  $1000 \text{ cm}^{-1}$ ). Contrarily, the H-non-containing molecules benefit from the localized characteristics of their torsional wavefunction, which arise from the proximity of the three local minimum depths. This feature would yield very long lifetimes owing to the predicted extremely narrow

TABLE III. Existing and optimized additional exponents for the O, F, Cl, Br, and I atoms of the dyall.3zp basis sets. The O's exponents were obtained in Ref. [70].

	O	F	Cl		Br	I
	$p$	$p$	$s$	$p$	$p$	$p$
second tightest	4.5531279E+01	5.8279110E+01	7.8714993E+05	4.7203082E+02	2.4820723E+04	1.1662681E+06
tightest	1.9430165E+02	2.4929585E+02	6.4063687E+06	2.1571374E+03	1.6203213E+05	7.5310209E+06
added	2.8126178E+03	5.1263846E+03	5.9958092E+07	3.6831954E+04	1.8253547E+06	5.4139599E+07
	1.9396596E+05	1.5303883E+04		1.3685631E+06	2.8240083E+07	
		2.8277597E+04		2.4578813E+07		

TABLE IV. Summary of the target molecules.

$R$ -configuration	$S$ -configuration
CHFCIOH	CFCIBrOH
CHFCBrOH	CFCIOH
CHFIOH	CFBrIOH
CHCIBrOH	CCIBrIOH
CHCIOH	
CHBrIOH	

linewidth.

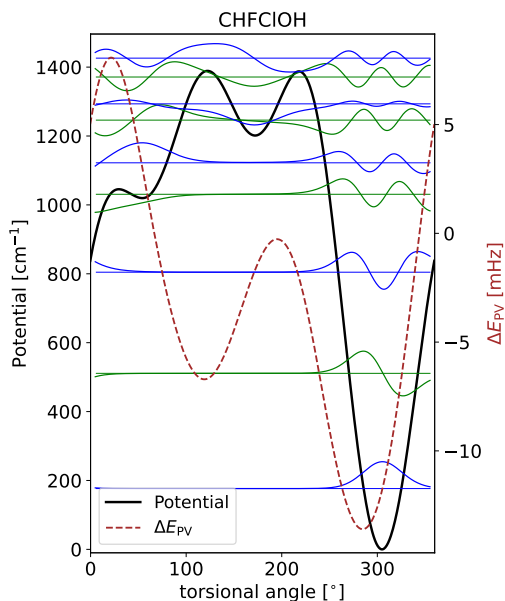


FIG. 5. Visualization of PECs (black solid line, left axis), 1D torsional wavefunctions (blue and green solid lines, left axis), and  $\Delta E_{PV}$  curves (brown dotted line, right axis) of *R*-CHFClOH. The  $\Delta E_{PV}$  at each torsional level is shown in Table V.

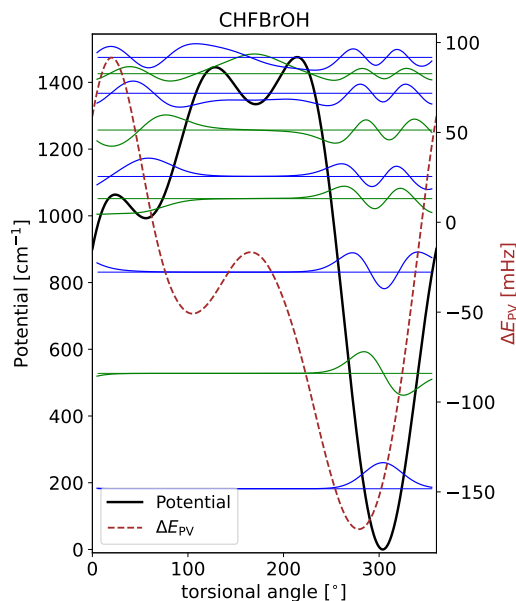


FIG. 6. Visualization of PECs (black solid line, left axis), 1D torsional wavefunctions (blue and green solid lines, left axis), and  $\Delta E_{PV}$  curves (brown dotted line, right axis) of *R*-CHFBrOH. The  $\Delta E_{PV}$  at each torsional level is shown in Table VI.

TABLE V. Vibrational energies ( $\tilde{\nu}$  in  $\text{cm}^{-1}$ ) referenced to the zero-point vibrational energy (#1) and PV frequency shift ( $\Delta\nu_{PV}$  in mHz) of *R*-CHFClOH.

CHFClOH					
#	$\nu_F$	$\nu_{Cl}$	$\nu_H$	$\tilde{\nu}$	$\Delta\nu_{PV}$
1	0	0	1	176.5	-10.84
2	0	0	2	334.5	-8.77
3	0	0	3	628.1	-6.13
4	0	0	4	854.3	-0.88
5	1	0	4	945.7	-0.29
6	1	0	5	1069.6	-2.24
7	0	1	0	1116.8	-2.46
8	2	1	5	1194.7	-2.94
9	-	-	-	1249.5	-3.40
10	-	-	-	1380.3	-2.89

TABLE VI. Vibrational energies ( $\tilde{\nu}$  in  $\text{cm}^{-1}$ ) referenced to the zero-point vibrational energy (#1) and PV frequency shift ( $\Delta\nu_{PV}$  in mHz) of *R*-CHFBrOH.

CHFBrOH					
#	$\nu_F$	$\nu_{Br}$	$\nu_H$	$\tilde{\nu}$	$\Delta\nu_{PV}$
1	0	0	1	182.0	-135.31
2	0	0	2	345.9	-113.57
3	0	0	3	649.3	-83.71
4	0	0	4	869.6	0.36
5	1	0	4	936.0	-28.90
6	1	0	5	1075.1	-27.02
7	2	0	5	1185.4	-43.66
8	2	1	5	1244.0	-27.36
9	-	-	-	1292.9	-46.38
10	-	-	-	1427.5	-38.58

## X. TORSIONAL QUANTUM NUMBER FOR THE CXYZOH MOLECULES

Traditionally, the quantum numbers at the vibrational ground states are defined as zero for all the vibrational modes. However, this convention would be insufficient in reflecting the character of the torsional wavefunction because ' $\nu_\tau = 0$ ' does not offer information on the bottom of the torsion potential at which the wavefunction is localized. Therefore, in this study, we defined the torsional quantum number as the number of the extremums of the vibrational wavefunction, except for the numerical noises, to clarify the character of the wavefunction.

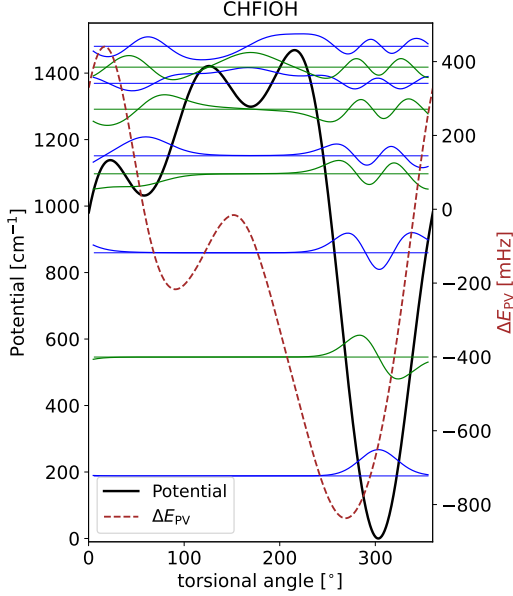


FIG. 7. Visualization of PECs (black solid line, left axis), 1D torsional wavefunctions (blue and green solid lines, left axis), and  $\Delta E_{PV}$  curves (brown dotted line, right axis) of *R*-CHFIOH. The  $\Delta E_{PV}$  at each torsional level is shown in Table VII.

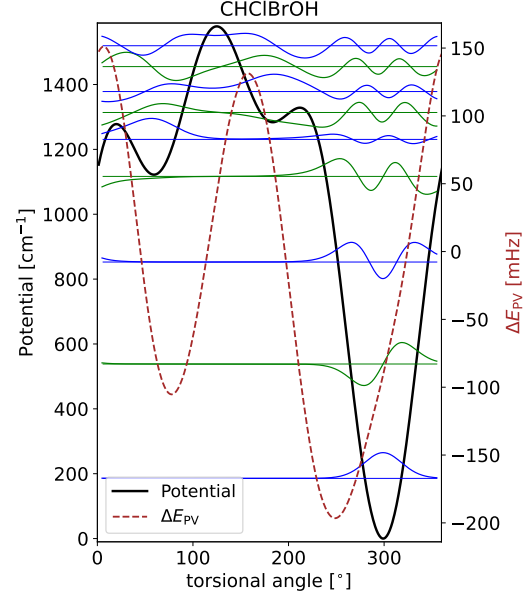


FIG. 8. Visualization of PECs (black solid line, left axis), 1D torsional wavefunctions (blue and green solid lines, left axis), and  $\Delta E_{PV}$  curves (brown dotted line, right axis) of *R*-CHClBrOH. The  $\Delta E_{PV}$  at each torsional level is shown in Table VIII.

TABLE VII. Vibrational energies ( $\tilde{\nu}$  in  $\text{cm}^{-1}$ ) referenced to the zero-point vibrational energy (#1) and PV frequency shift ( $\Delta\nu_{PV}$  in mHz) of *R*-CHFIOH.

CHFIOH					
#	$\nu_F$	$\nu_I$	$\nu_H$	$\tilde{\nu}$	$\Delta\nu_{PV}$
1	0	0	1	188.2	-603.57
2	0	0	2	357.6	-522.90
3	0	0	3	671.3	-406.44
4	0	0	4	908.9	-63.08
5	1	0	4	963.0	-154.39
6	2	0	4	1103.2	-125.74
7	2	1	4	1181.1	-166.44
8	2	1	5	1229.7	-172.83
9	-	-	-	1292.5	-225.94
10	-	-	-	1422.9	-181.43

TABLE VIII. Vibrational energies ( $\tilde{\nu}$  in  $\text{cm}^{-1}$ ) referenced to the zero-point vibrational energy (#1) and PV frequency shift ( $\Delta\nu_{PV}$  in mHz) of *R*-CHClBrOH.

CHClBrOH					
#	$\nu_{Cl}$	$\nu_{Br}$	$\nu_H$	$\tilde{\nu}$	$\Delta\nu_{PV}$
1	0	0	1	185.5	-87.84
2	0	0	2	352.7	-80.38
3	0	0	3	667.1	-68.46
4	0	0	4	931.1	-47.54
5	1	0	4	1045.2	-32.28
6	1	0	5	1128.2	-43.21
7	1	1	5	1192.8	28.58
8	2	1	5	1269.7	-11.72
9	-	-	-	1334.0	-1.29
10	-	-	-	1458.2	-0.47

## XI. COMPARISON WITH CAM-B3LYP\* FUNCTIONAL

The enhancement mechanism is also examined using another DFT functional optimized for  $\Delta E_{\text{PV}}$  (the contribution only from Br and Cl atoms) in CHFClBr at the CCSD(T) level, which is noted as CAM-B3LYP\* [78].

In the CAM-B3LYP approximation [88–90], electron-electron Coulomb operator into a short-range density functional and a long-range wave-function-based part is expressed by

$$V_{\text{ee}} = \sum_{i<j} \frac{1 - [\alpha + \beta \operatorname{erf}(\mu r_{ij})]}{r_{ij}} + \sum_{i<j} \frac{\alpha + \beta \operatorname{erf}(\mu r_{ij})}{r_{ij}}, \quad (11)$$

where  $r_{ij}$  is the distance between two electrons  $i$  and  $j$ ,  $\alpha = 0.20$ ,  $\beta = 0.12$ , and  $\mu = 0.90$  are the parameters optimized in Ref. 78.

The comparison between the CAM-B3LYP\* and PBE0 functionals is shown in Table XI. The maximum deviation is  $-0.12$  mHz ( $\tau = 306^\circ$ ), which is much smaller than the maximum absolute  $\Delta E_{\text{PV}}$  value shown at  $\tau = 288^\circ$ ,

$-6.86$  ( $-6.77$ ) mHz at the CAM-B3LYP\* (PBE0) functionals. The maximum difference in the PEC is relatively large ( $-57.6$   $\text{cm}^{-1}$  at  $\tau = 234^\circ$ ), but the torsional angles that show the local minimum and maximum are very similar.

Table XII lists the PV frequencies and vibrational energies calculated with the CAM-B3LYP\* and PBE0 functionals. The relative difference of  $\Delta\nu_{\text{PV}}$  becomes large when its absolute value of  $\Delta\nu_{\text{PV}}$  is close to zero (e.g., #4 and #5). However, the differences ( $\Delta$ ) are smaller than the most sensitive transition to the PV (between #1 and #5,  $\sim 11$  mHz). In the states in which the vibrational wavefunction is plane-wave-like (i.e., high-energy vibrational states), the values of  $\Delta\nu_{\text{PV}}$  at the CAM-B3LYP\* and PBE0 levels are very close. From this and the comparison shown in Table XI, the difference between CAM-B3LYP\* and PBE0 would be mainly due to the vibrational wavefunction. Although the benchmark data is not reported for the CAM-B3LYP\*, the validity of the PBE0 function for the torsional PEC is assessed in Ref [76].

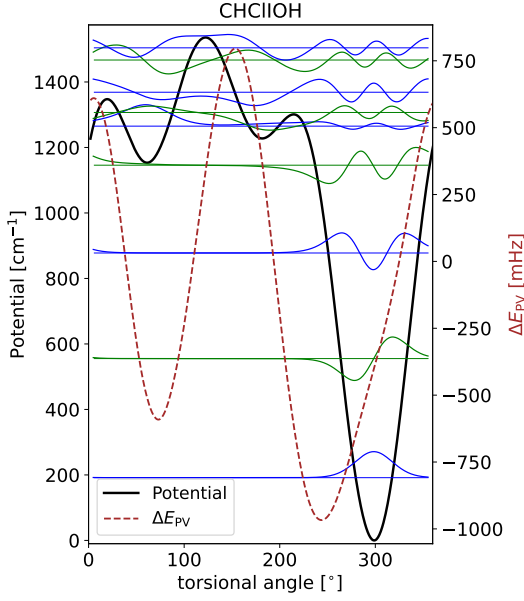


FIG. 9. Visualization of PECs (black solid line, left axis), 1D torsional wavefunctions (blue and green solid lines, left axis), and  $\Delta E_{PV}$  curves (brown dotted line, right axis) of *R*-CHClOH. The  $\Delta E_{PV}$  at each torsional level is shown in Table IX.

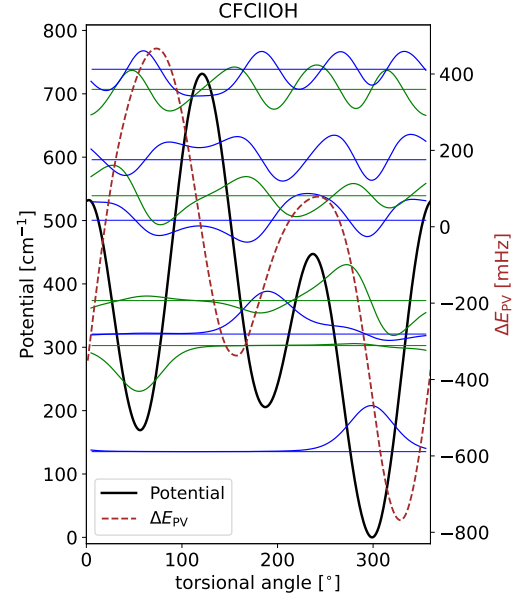


FIG. 10. Visualization of PECs (black solid line, left axis), 1D torsional wavefunctions (blue and green solid lines, left axis), and  $\Delta E_{PV}$  curves (brown dotted line, right axis) of *S*-CFClOH. The  $\Delta E_{PV}$  at each torsional level is shown in Table X.

TABLE IX. Vibrational energies ( $\tilde{\nu}$  in  $\text{cm}^{-1}$ ) referenced to the zero-point vibrational energy (#1) and PV frequency shift ( $\Delta\nu_{PV}$  in mHz) of *R*-CHClOH.

CHClOH						
#	60	180	300	$\tilde{\nu}$	$\Delta\nu_{PV}$	
	$\nu_{Cl}$	$\nu_I$	$\nu_H$			
1	0	0	1	191.6	-396.41	
2	0	0	2	363.7	-384.84	
3	0	0	3	686.1	-359.17	
4	0	0	4	954.3	-316.16	
5	1	0	0	1073.5	-305.51	
6	1	1	4	1115.2	-48.16	
7	1	1	5	1177.1	46.05	
8	2	1	5	1275.4	-96.26	
9	2	2	5	1312.6	61.83	
10	-	-	-	1448.7	-13.87	

TABLE X. Vibrational energies ( $\tilde{\nu}$  in  $\text{cm}^{-1}$ ) referenced to the zero-point vibrational energy (#1) and PV frequency shift ( $\Delta\nu_{PV}$  in mHz) of *S*-CFClOH.

CFClOH						
#	60	180	300	$\tilde{\nu}$	$\Delta\nu_{PV}$	
	$\nu_{Cl}$	$\nu_I$	$\nu_F$			
1	0	0	1	135.3	-412.04	
2	1	0	0	167.4	352.51	
3	0	1	0	185.6	-126.32	
4	0	1	2	238.4	-332.21	
5	2	2	2	365.2	-126.10	
6	-	-	-	403.9	75.32	
7	-	-	-	460.7	-169.53	
8	-	-	-	571.8	-110.53	
9	-	-	-	603.5	-47.60	
10	-	-	-	757.2	-91.68	

TABLE XI.  $\Delta E_{PV}$  and PEC of CHFC1OH obtained with CAM-B3LYP\* and PBE0 functionals based on the eAMF-X2C Hamiltonian (with the Gaunt term) as a function of torsional angles. The dyall.3zp basis set with tight exponents is used. The differences between the two functionals ( $\Delta$ ) are also listed. The geometries were optimized at the PBE1PBE/Def2TZVPP level.

$\tau$	$\Delta E_{PV}$ (mHz)			PEC ( $\text{cm}^{-1}$ )		
	CAM-B3LYP*	PBE0	$\Delta$	CAM-B3LYP*	PBE0	$\Delta$
0	2.50	2.51	-0.01	865.2	837.5	27.7
9	3.51	3.50	0.01	979.9	953.2	26.7
18	4.03	4.00	0.03	1044.4	1020.0	24.3
27	3.99	3.95	0.04	1066.1	1044.4	21.7
36	3.49	3.45	0.04	1058.7	1040.9	17.8
45	2.63	2.59	0.04	1042.4	1027.7	14.7
54	1.58	1.55	0.03	1031.8	1019.7	12.1
63	0.49	0.47	0.02	1039.9	1030.6	9.3
72	-0.52	-0.53	0.01	1074.8	1068.6	6.2
81	-1.44	-1.43	-0.01	1131.9	1128.1	3.8
90	-2.20	-2.18	-0.02	1204.0	1202.6	1.4
99	-2.80	-2.77	-0.03	1278.5	1279.5	-1.0
108	-3.20	-3.16	-0.04	1340.2	1343.3	-3.2
117	-3.38	-3.34	-0.04	1376.3	1381.6	-5.3
126	-3.34	-3.30	-0.04	1379.9	1387.3	-7.4
135	-3.08	-3.05	-0.03	1352.8	1362.2	-9.4
144	-2.63	-2.61	-0.02	1304.2	1315.7	-11.5
153	-2.06	-2.06	0.00	1249.0	1263.2	-14.2
162	-1.45	-1.47	0.02	1203.1	1220.8	-17.7
171	-0.87	-0.91	0.04	1179.5	1201.7	-22.2
180	-0.41	-0.47	0.06	1184.3	1212.3	-27.9
189	-0.11	-0.19	0.08	1216.1	1250.4	-34.3
198	-0.06	-0.15	0.09	1263.2	1305.2	-42.0
207	-0.28	-0.37	0.09	1309.7	1358.1	-48.4
216	-0.80	-0.88	0.08	1332.8	1386.8	-54.0
225	-1.61	-1.68	0.07	1312.6	1369.8	-57.2
234	-2.63	-2.68	0.05	1234.1	1291.7	-57.6
243	-3.78	-3.81	0.03	1093.3	1149.6	-56.3
252	-4.87	-4.87	0.00	902.9	954.3	-51.4
261	-5.79	-5.77	-0.03	683.3	727.6	-44.4
270	-6.47	-6.41	-0.05	460.5	496.4	-35.9
279	-6.83	-6.75	-0.08	262.9	289.4	-26.6
288	-6.86	-6.77	-0.10	111.0	128.0	-17.0
297	-6.56	-6.45	-0.11	20.2	27.5	-7.3
306	-5.91	-5.80	-0.12	2.4	0.7	1.7
315	-4.93	-4.82	-0.11	55.3	45.6	9.7
324	-3.66	-3.56	-0.10	170.4	153.5	17.0
333	-2.15	-2.07	-0.09	332.8	310.3	22.5
342	-0.51	-0.45	-0.06	519.8	493.8	26.0
351	1.10	1.13	-0.03	705.7	678.1	27.6
360	2.50	2.51	-0.01	865.2	837.5	27.7

TABLE XII. Vibrational energies ( $\tilde{\nu}$  in  $\text{cm}^{-1}$ ) referenced to the zero-point vibrational energy (#1) and PV frequency shift ( $\Delta\nu_{\text{PV}}$  in mHz) of *R*-CHFClOH. The  $\Delta E_{\text{PV}}$  curve and PEC shown in Table XI are used for the vibrational computations. The states are assigned referring to FIG. 5 .

	60 180 300			$\tilde{\nu}$ ( $\text{cm}^{-1}$ )			$\Delta\nu_{\text{PV}}$ (mHz)		
	F	Cl	H	CAM-B3LYP*	PBE0	$\Delta$	CAM-B3LYP*	PBE0	$\Delta$
1	0	0	1	176.0	176.5	-0.6	-11.25	-10.84	-0.41
2	0	0	2	333.4	334.5	-1.1	-9.18	-8.77	-0.41
3	0	0	3	626.6	628.1	-1.6	-6.60	-6.13	-0.47
4	0	0	4	857.6	854.3	3.3	-1.75	-0.88	-0.88
5	1	0	4	950.6	945.7	4.9	0.28	-0.29	0.57
6	1	0	5	1065.0	1069.6	-4.6	-2.22	-2.24	0.02
7	0	1	0	1094.2	1116.8	-22.7	-2.18	-2.46	0.28
8	2	1	5	1187.1	1194.7	-7.6	-2.75	-2.94	0.19
9	-	-	-	1231.5	1249.5	-18.0	-3.37	-3.40	0.03
10	-	-	-	1368.8	1380.3	-11.5	-2.84	-2.89	0.06
11	-	-	-	1382.0	1395.7	-13.7	-3.18	-3.20	0.02
12	-	-	-	1597.2	1608.5	-11.3	-2.98	-3.04	0.06
13	-	-	-	1598.4	1609.9	-11.5	-3.03	-3.04	0.02
14	-	-	-	1870.7	1881.4	-10.7	-3.05	-3.08	0.03
15	-	-	-	1870.8	1881.6	-10.8	-3.04	-3.07	0.03
16	-	-	-	2191.2	2201.5	-10.4	-3.09	-3.12	0.02
17	-	-	-	2191.2	2201.6	-10.4	-3.09	-3.11	0.02
18	-	-	-	2557.6	2567.7	-10.1	-3.14	-3.15	0.02
19	-	-	-	2557.7	2567.8	-10.1	-3.13	-3.15	0.02
20	-	-	-	2969.2	2979.2	-9.9	-3.17	-3.18	0.01